The Astrophysical Journal, 913:59 (10pp), 2021 May 20 https://doi.org/10.3847/1538-4357/abf2b9

High-resolution He I 10830 Å Narrowband Imaging for a Small-scale Chromospheric Jet

Ya Wang[1,2], Qingmin Zhang[1,3], and Haisheng Ji[1,3]
[1] Key Laboratory of Dark Matter and Space Astronomy, CAS, Nanjing 210023, People's Republic of China; wangya@pmo.ac.cn, jihs@pmo.ac.cn
[2] Key Laboratory for Modern Astronomy and Astrophysics (Nanjing University), Ministry of Education, Nanjing 210023, People's Republic of China
[3] School of Astronomy and Space Science, University of Science and Technology of China, Hefei 230026, People's Republic of China
Received 2020 September 23; revised 2021 March 24; accepted 2021 March 25; published 2021 May 25

Abstract

Solar jets are ubiquitous phenomena in the solar atmosphere. They are important in mass and energy transport to the upper atmosphere and interplanetary space. Here, we report a detailed analysis of a small-scale chromospheric jet with high-resolution He I 10830 Å and TiO 7057 Å images observed by the 1.6 m aperture Goode Solar Telescope at the Big Bear Solar Observatory. The observation reveals the finest dark threads inside the jet are rooted in the intergranular lanes. Their width is equal to the telescope's diffraction limit at 10830 Å (∼100 km). The jet is recurrent and its association with the emergence and convergence of magnetic flux is observed. Together with other important features like photospheric flow toward the magnetic polarity inversion line, a bald-patch magnetic configuration, and earlier excitation of helium atoms, we propose that the jet might be initiated by magnetic reconnection in a U-shaped loop configuration. The plasmoid configuration results from the possible buoyancy of the magnetic reconnection, which reoccurs in a second step with an overlying magnetic field line. Notably, the second-step magnetic reconnection produces not only bidirectional cool or hot flows but also a new U-shaped loop configuration. The feature may be used to explain the recurrent behavior of the jet, since the new U-shaped loop can be driven to reconnect again.

Unified Astronomy Thesaurus concepts: Solar chromosphere (1479); Solar magnetic reconnection (1504)

Supporting material: animation

1. Introduction

Solar jets are one of the transient phenomena that frequently occur in the solar atmosphere. They are observed as collimated ejecting plasma beams along magnetic field lines and play an important role in the mass and energy transport, coronal heating, and acceleration of the solar wind (e.g., Tian et al. 2014). The earliest observations of solar jets can date back to the 1940s. Major advances have been made in both observational and theoretical aspects over the past few decades. The unceasing improvements in space mission and ground-based telescopes provide more and more details on their initiation and evolution (Raouafi et al. 2016; Shen 2021 and references therein). The jet-like phenomena observed in the chromospheric Hα line are called Hα surges (Roy 1973a). Multiwavelength observations show that Hα surges are often associated with extreme ultraviolet (EUV) and even soft X-ray emissions, with coexisting cool and hot components. But the cool and hot emissions are not always co-spatial (Jiang et al. 2007; Zhang & Ji 2014), and their physical parameters are quite different. The hot components or so-called coronal jets have speeds of 90−310 km s^{-1}, lifetimes of 100−2000 s, sizes of (1.1−5.0) × 10^5 km, and widths of 10^3–10^4 km (Kim et al. 2007; Nistcò et al. 2009). Here, the width refers to the transverse spatial scale of the jet envelope, rather than to the fine structure of the jets. For chromospheric jets, the typical parameters of length, width, lifetime, and velocity are in the ranges of 1−4 Mm, 100−400 km, 100−500 s, and 5−20 km s^{-1}, respectively (Nishizuka et al. 2011). The discrepancy comes from the different yet coupled physical processes (e.g., Shibata et al. 2007), and we need further well-observed events to reveal the coupling.

Hα and Ca II spectral lines are widely used to detect chromospheric jets (e.g., Shibata et al. 2007; Nishizuka et al. 2011). However, the observation of jets in the He I 10830 Å passband is quite rare. This passband is special since it is formed in the upper chromosphere and is sensitive to EUV emissions from the transition region located above. The He I 10830 Å line is formed by transitions between the metastable level 1s2s (3S) and the closely spaced 1s2p (3P) triplet level in He triplet atoms (orthohelium). The lowest metastable level of orthohelium has a high excitation energy of 19.77 eV. The formation mechanisms include photoionization followed by recombination (the PRM mechanism; Zirin 1975; Golding et al. 2014; Wang et al. 2016), collisional ionization followed by reconnection (the CRM mechanism), and direct collisional excitation by high-temperature electrons or nonthermal electrons during flares (the CM mechanism; Ding et al. 2003). He I 10830 Å has proven to be an ideal window for studying the coupling process between the hot and cool components (Ji et al. 2012; Hong et al. 2017; Hashim et al. 2020). High-resolution He I 10830 Å observation has unveiled jet characteristics that could not be observed with lower spatiotemporal resolution or other passbands (Zeng et al. 2013, 2016).

Chromospheric jets often show a cusp or inverted Y shaped structure, and this kind of chromospheric jet is described by Shibata et al. (2007) as a chromospheric anemone jet. X-ray jets also tend to have an anemone shape at their footpoints, which are mostly located in magnetic mixed-polarity regions (Shimojo et al. 1996, 1998). The bright inverted Y structures provide evidence of magnetic reconnection between an emerging magnetic bipole and an ambient preexisting field, frequently in the form of a fan–spine magnetic topology (Liu et al. 2011; Zhang & Zhang 2017; Zeng et al. 2016). Since the topology is formed through magnetic flux emergence (Liu et al. 2011), jets are tightly related to the evolution of an underlying magnetic field (Cheung et al. 2015). Observations show that jets tend to occur above satellite sunspots, small

opposite-polarity magnetic elements, and regions of moving magnetic features (e.g., Rust 1968; Roy 1973b). Sometimes, the magnetic variations show magnetic flux emergence, followed by flux cancellation (e.g., Shen et al. 2012; Sterling et al. 2018). Occasionally, jets are associated with magnetic flux cancellations caused by the converging and shearing motions of the opposite polarities (e.g., Shen et al. 2012; Panesar et al. 2016, 2018). They are recurrent and the recurrence results from periodic magnetic reconnections (Guo et al. 2013; Hu et al. 2015; Liu et al. 2016). The periodic magnetic reconnection may be ultimately related to the photosphere. As we step into the era of high-resolution observations with meter-aperture telescopes, the investigation of the dynamic properties of the finest structures in the photosphere during a jet event becomes feasible and deserves our further attention. Using high-resolution He I 10830 Å observations of a small-scale recurrent jet event near the solar limb, Zeng et al. (2016) reported evidence of fan–spine reconnection in the event. However, they could not reveal what was occurring in the photosphere due to limb shortening.

In this paper, we focus on the analysis of a small-scale jet on the northern side of the sunspot in active region 12127 on 2014 August 1, with high-resolution narrowband images at 10830 Å and broadband images at TiO 7057 Å. For this active region, solar activity as revealed by high-resolution observations (e.g., flares, jets, umbral rotation) is abundant and interesting, and a number of results have been reported in the literature (Bai et al. 2016; Su et al. 2016; Liu & Su 2018). The data and instruments are briefly described in Section 2. Section 3 presents the observations and analysis. Sections 4 and 5 present a discussion and summary, respectively.

2. Data and Instruments

The data set analyzed in this study mainly consists of TiO 7057 Å and He I 10830 Å obtained from the Goode Solar Telescope (GST) at Big Bear Solar Observatory (BBSO), EUV/UV passbands from the Atmospheric Imaging Assembly (AIA; Lemen et al. 2012), and magnetograms from the Helioseismic and Magnetic Imager (HMI; Schou et al. 2012) on board SDO. GST has an off-axis design, which can eliminate any central obscuration, reducing stray light (Cao et al. 2010a; Goode et al. 2010a). Long duration, good seeing conditions, and a high-order adaptive optics system are beneficial to obtaining diffraction-limited images for hours. High spatial resolution images were obtained by using a broadband filter (bandpass: 10 Å), including TiO 7057 Å, and a narrowband filter in He I 10830 Å. The TiO 7057 Å line has a pixel size of $0\farcs034$ using the Broadband Filter Imager. A high-sensitivity HgCdTe CMOS infrared focal plane array camera (Cao et al. 2010b) was utilized to obtain the 10830 Å data. The 10830 Å data have a pixel size of $\sim 0\farcs08$, a cadence of ∼10 s, and a field of view (FOV) of about $90'' \times 90''$.

The EUV counterparts of the jet were observed by SDO/AIA, with a pixel size of $0\farcs6$ and a cadence of 12 s, covering a broad temperature range (from ∼1 MK to ∼10 MK). SDO/AIA also provides UV images in 1600 Å (C IV+continuum, $\log T \sim 5.0$) and 1700 Å (continuum, $\log T \sim 3.7$). The magnetograms were provided by HMI on board SDO. The full-disk, line-of-sight magnetograms have a cadence of 45 s. The vector magnetograms obtained from the Space-weather HMI Active Region Patches data series have a cadence of 720 s. The data sets from BBSO/GST and SDO were co-aligned using the cross-correlation method.

3. Observation and Data Analysis

3.1. Dynamic Process of the Hot and Cool Components

An overview of the jet is depicted in Figure 1 and its online animation (f1animation.mp4). Using the observation from 10830 Å imaging, we first compare the dynamic process (a2) and the time profile (a1). We note that the jet is recurrent, and divide it into six stages. The counterpart results from AIA are presented in panel (b1) and panels (c2)–(e2). From the online animation, we can see that UV or EUV emissions are present during all the stages. In Figure 1, the FOV of integration for all lightcurves encompasses the entire jet in the 10830 Å images during its maximum phase (∼18:05). In this way, the UV and EUV emissions fall into the noise levels in the lightcurves during stages 1 and 6 due to the larger integration FOV compared with the size of the UV/EUV emissions. In other words, these stages are dominated by cool material ejections. We will focus on stages 2 and 4. Figure 2 shows the images at 10830, 1600, 304, and 131 Å during stages 1, 2, and 4.

In the 10830 Å images, the jet, with a size of $\sim 10'' \times 10''$, shows a spire and a dome-like structure that is hidden inside and below. The online animation shows not only the ejection along the spire, whose direction is indicated by red dashed lines in Figure 2(d2), but also the elevation and rotation of magnetic arcades that constitute the dome-like structure. The UV and EUV emissions are more compact, only appearing in the upper part of the spire and giving an apparent collimated ejection. Note that there is a transverse offset between the cool and hot ejections.

Although the jet manifests absorption in He I 10830 Å, brightenings are observed inside the dome (panel (b1) of Figure 2). In 1600 Å (panel (b2) of Figure 2), the jet presents an inverted Y structure with bright kernels at the bottom. The bright kernels are associated with the 10830 Å emission inside the dome in both space and time. At the time of rapid enhancement of the EUV emission in stage 4, there is an obvious downward motion of cool materials, whose position and direction are depicted with blue arrows in panels (a2) and (c2) of Figure 1 and panels (c1) and (d1) of Figure 2. During the bidirectional flows, the dome-like structure changes to a simple vertical structure (see the online animation and Figure 2).

To study the apparent speed of the jet and the downward motion, we plot the spacetime diagrams along the spire (slit 1; red line in Figure 2) and base (slit 2; green line in Figure 2) in Figure 3. The bright kernel located at the base (or inside the dome) moves earlier to subsequent ejection, at a speed of ∼(38 −64) km s^{-1} as observed in SDO/AIA 1600 Å, 1700 Å, and 304 Å. However, the ejection itself has a faster outward movement at a speed of ∼255 km s^{-1} (panels (e)−(f)). For the He I 10830 Å observation, the chromospheric jet ejects at a moderate speed of 98.2 km s^{-1}. The He I 10830 Å diagrams unambiguously display downward motion (panels (a)−(b)). Especially in stages 3 and 4, the materials move up and down almost simultaneously. The velocity of the downward motion is about 27.7 km s^{-1}. Moreover, the apparent length of the spire in the EUV passbands is about $(5-7) \times 10^3$ km. However, in the He I 10830 Å passband, the apparent length of the dark threads is about $(1.0-1.5) \times 10^4$ km, and the length of the

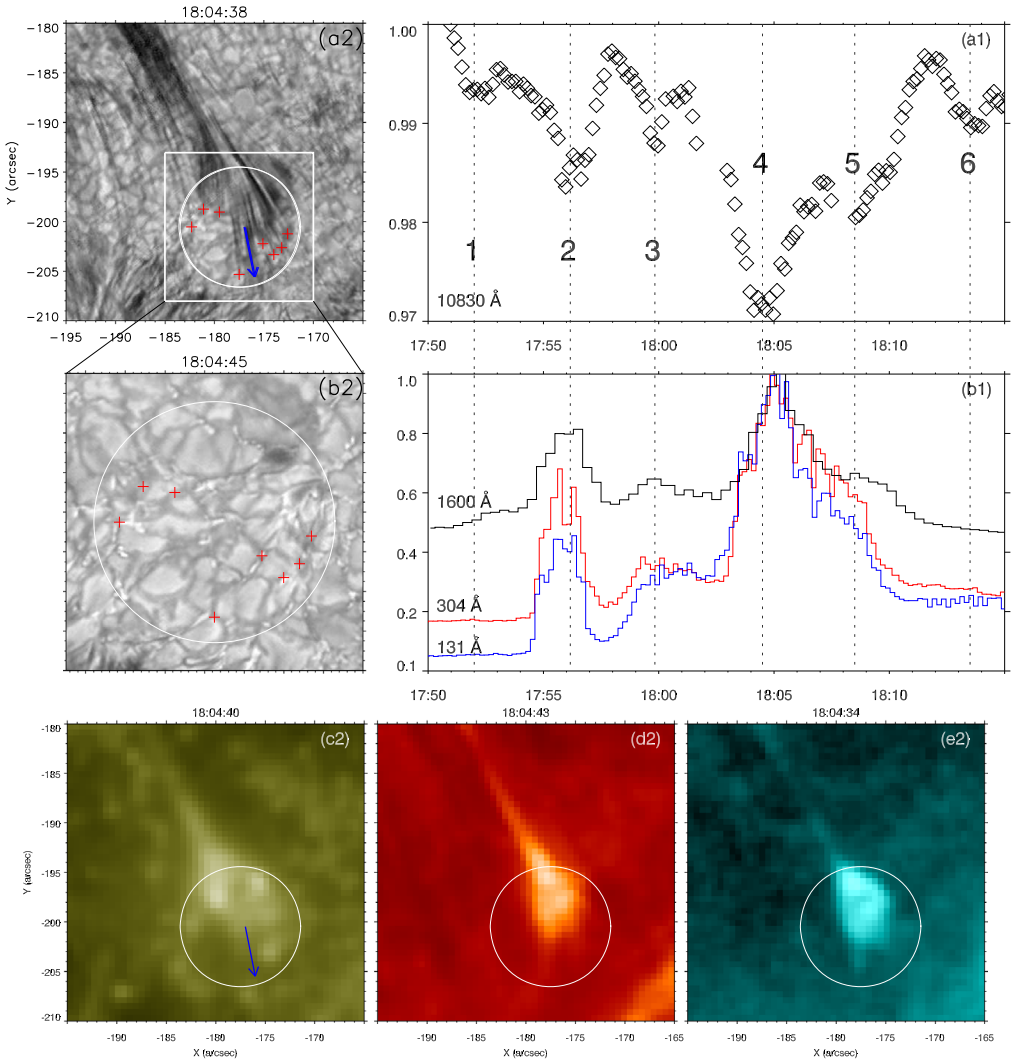

Figure 1. Snapshots of the jet at 10830, 1600, 304, and 131 Å are given in panels (a1) and (c2)–(e2), while panel (b2) gives an enlarged view for the underlying photosphere as observed at 7057 Å. The circles highlight the base of the jet. The plus signs display the locations where some of the dark threads of the jet are rooted in intergranular lanes. Panels (a1)–(b1) give the time profiles for the normalized integrated intensity around the region of the jet at 10830, 1600, 304, and 131 Å. The dotted lines show the peak time in the six stages of the jet. The blue arrows show the downflow along the newly formed magnetic lines. An animation of this figure is available. The animation begins at approximately 17:51 and ends at 18:15. The real-time duration of the animation is 11 s.

(An animation of this figure is available.)

dome is about $(3-5)\times10^3$ km. The different parameters clearly show the differences between the cool and hot materials.

3.2. Photospheric Evolution and Magnetic Structure

We use high-resolution photosphere images observed with GST and vector magnetograms observed with HMI. A snapshot of the photosphere below the jet with an enlarged image is shown in panel (b2) of Figure 1 (also see the online animation). We find that the photospheric evolution and magnetic activity associated with the jet are apparent, as shown in Figure 4. The jet is related to a small region of the negative magnetic field (panels (a)–(c)). Several negative poles concentrate, move toward the northwest, and push the polarity inversion line (PIL). In the corresponding TiO images (panels (d)–(f)), we observe the formation and evolution of dark fibrils indicated with boxes, which are analogous to discrete penumbra structures but between granulations.

By utilizing the differential affine velocity estimator for vector magnetograms (DAVE4VM; Schuck 2008) and Fourier local correlation tracking (Welsch et al. 2004), we can obtain the differential affine velocity and horizontal plasma velocity, based on the vector magnetic field data and TiO data. The image sequences used for velocity calculation are from 18:01 UT to 18:04 UT. The velocity estimated from the vector magnetic field is indicated by arrows in Figures 4(a)–(c). The average velocity in the black box is about 150 m s^{-1}. However, the plasma velocity in the region of the jet based on TiO data is estimated to be 100 m s^{-1}. In the enlarged view (panel (f) of Figure 4) of the black boxes, the TiO image is overlaid with the contours of the magnetogram. The flow converges into dark fibrils and squeezes toward the PIL.

Figure 5 gives snapshots of vector magnetograms during the jet as observed by HMI. To study the variation of the magnetic flux, we integrated the magnetic field along the line of sight over the region of the jet, which is indicated by black boxes in Figure 5. As shown in Figure 6, the positive, negative, and total

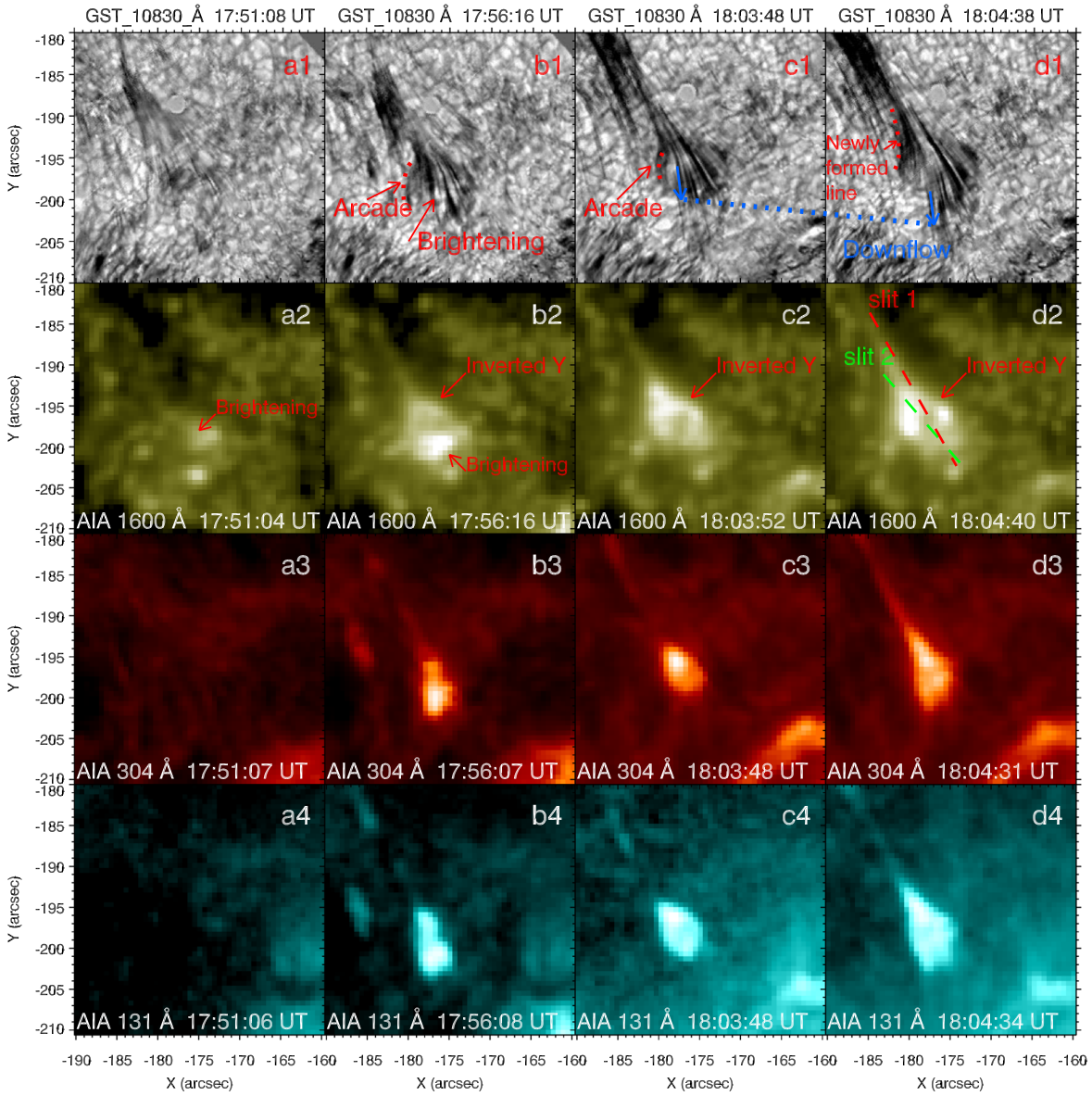

Figure 2. An extension of Figure 1, showing the different morphologies of the jet at the 10830, 1600, 304, and 131 Å passbands and at 17:51 UT, at 17:56 UT, and before and after 18:04 UT. Slits 1 and 2 in panel (d2) indicate the positions used to make the spacetime diagrams in Figure 3.

magnetic fluxes increase within 50 minutes before the jet. However, at ∼17:50 UT, the positive and total magnetic fluxes suddenly decrease. On the other hand, the total intensity of the horizontal magnetic field in the same region increases after 17:50 UT, shown in panel (d). The enhancement of the horizontal magnetic field during the jet is also presented in Figure 5. It is clear that the horizontal magnetic field starts from negative polarity and changes to positive polarity across the PIL, which is evidence of a bald-patch topology.

To obtain the magnetic topology of the jet, we performed nonlinear force-free field (NLFFF) extrapolation by using the optimization approach proposed by Wheatland et al. (2000) and implemented by Wiegelmann (2004). For the bottom boundary, we use the HMI vector magnetogram of the jet region retrieved from the HMI.sharp_720 s data series before the jet's occurrence (∼17:48 UT). The 180° ambiguity in the transverse components of the vector magnetic field is resolved by the improved minimum energy method (Metcalf et al. 2006; Leka et al. 2009). The dimensions for the extrapolation are $204 \times 126 \times 204$ Mm^3. The jet's region is just part of the extrapolation area. The result is shown in Figure 7. The magnetic topology seen from the Z-direction matches the jet based on our observation (panel (a)). However, from the side view (panel (b)), we find that the field lines have dips tangential to the photosphere across the PIL, which is indicated by white curves in the figure.

4. Discussion

For this jet, the formation of 10830 Å absorption may be complicated. At the beginning of each stage, 10830 Å absorption enhancement occurs prior to the EUV emissions, which is shown in the lightcurves in Figure 1 and in the associated animation. Certainly, the 10830 Å absorption is associated with EUV emissions from the corona during peak time periods. Since absorption is also proportional to the density of He atoms, one possibility is that, under EUV illumination from the surrounding area, He atoms contained in

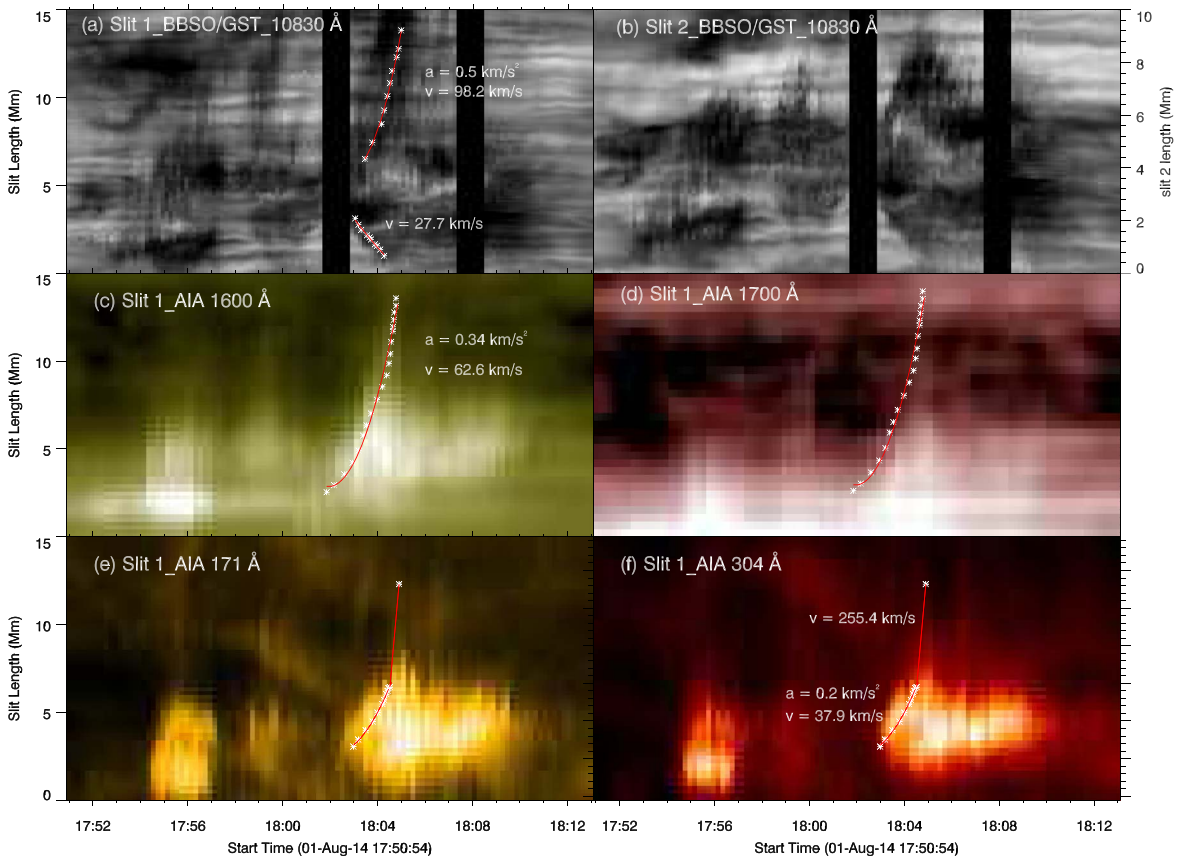

Figure 3. Panels (a) and (b) display the spacetime diagrams obtained by stacking intensity images in the He I 10830 Å passband along the paths of the jet marked by red (slit 1) and green (slit 2) dotted lines in Figure 2(d2). The paths of the jet are depicted by asterisks. The two black periods are due to the lack of 10830 Å observations. Panels (c)–(f) show the spacetime diagrams obtained by stacking intensity images in EUV/UV passbands along slit 1. The paths of the jet are depicted by asterisks along the edge of the path.

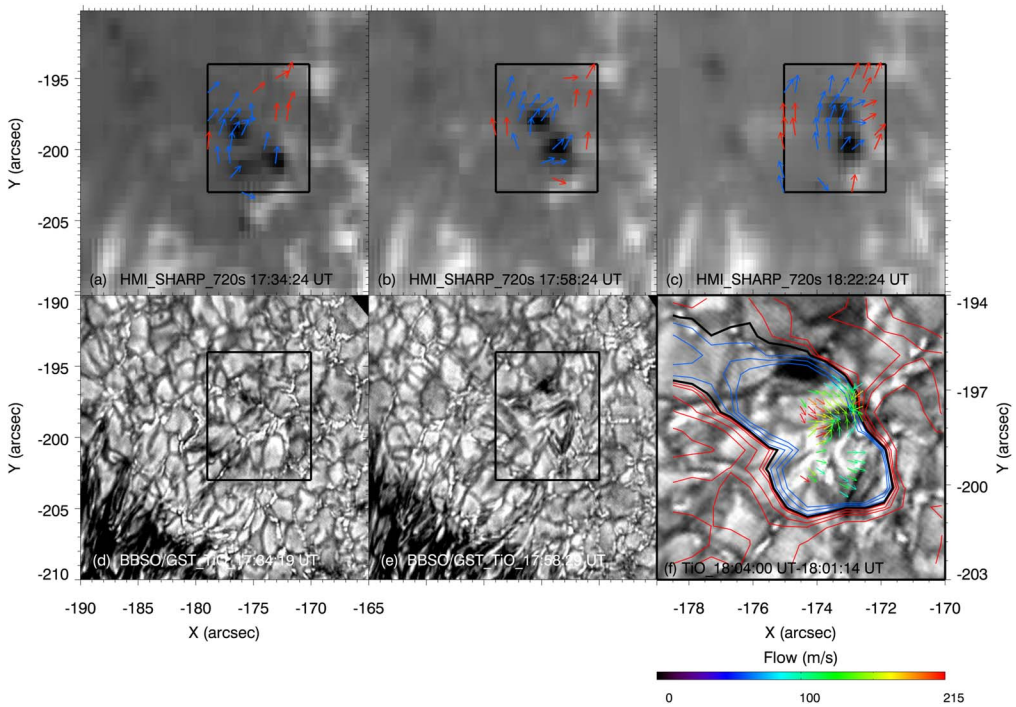

Figure 4. Top panels (a)–(c): snapshots of magnetograms for vertical magnetic field observed by HMI_sharp_720 s data series. The blue and red arrows represent the velocity on the negative field and positive field, respectively. Bottom panels (d)–(e): evolution of dark fibrils on the photosphere observed in TiO 7057 Å. The black boxes indicate the base region of the jet. Panel (f) displays an enlarged view of the photosphere image in the black boxes, which is overlaid with the contours of the vertical magnetic field. The arrows represent the photospheric flow obtained from photospheric data.

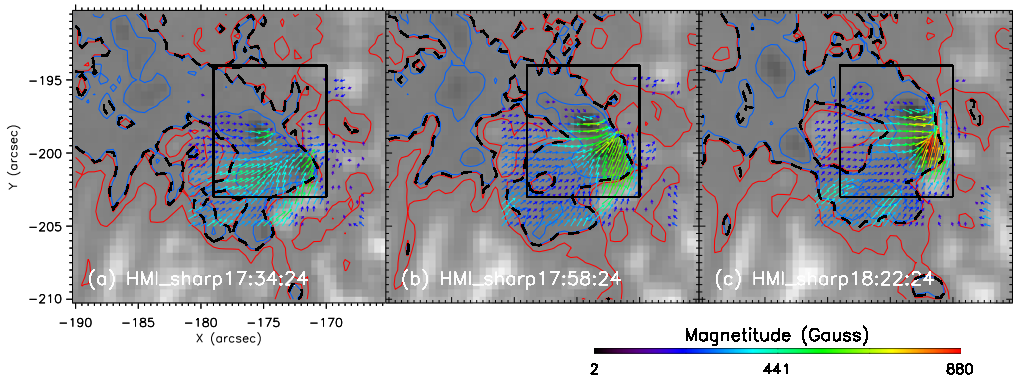

Figure 5. Three vector magnetograms obtained from the HMI_sharp_720 s data series. The arrows represent the transverse magnetic field. The black dashed lines indicate the PIL, while the red and blue contours indicate the positive magnetic field from 5 and 50 G and the negative magnetic field from −5 and −50 G, respectively. The black boxes show regions where the time profiles of the magnitude of the transverse magnetic field (given in Figure 6) are integrated.

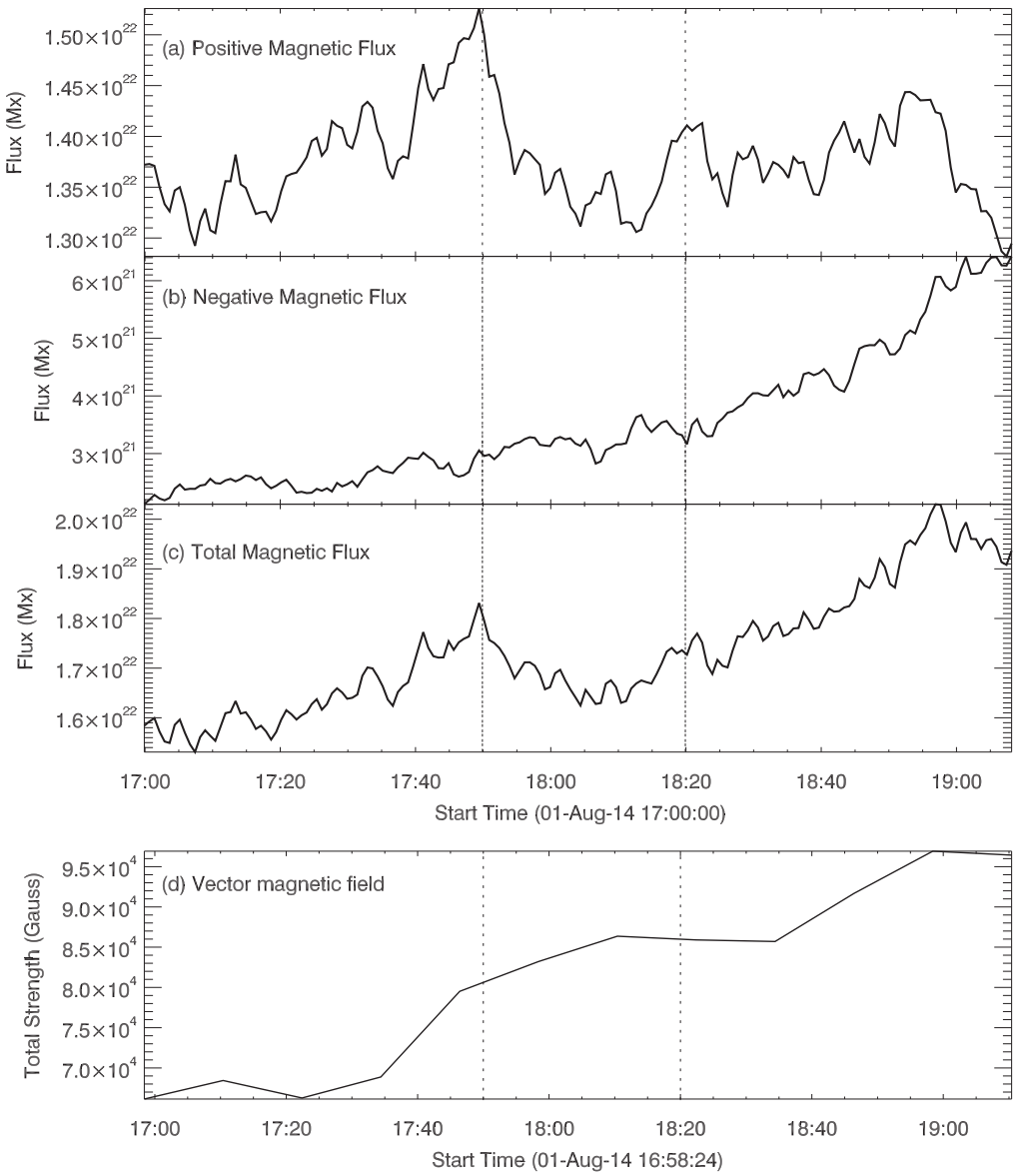

Figure 6. The time profiles of the positive magnetic flux (a), negative magnetic flux (b), and total magnetic flux (c) integrated over the region marked as black boxes in Figure 5. Panel (d) shows the time profile of the magnitude of the transverse magnetic field. The two dotted lines indicate 17:50 UT and 18:20 UT, which is the time range of the small-scale jet.

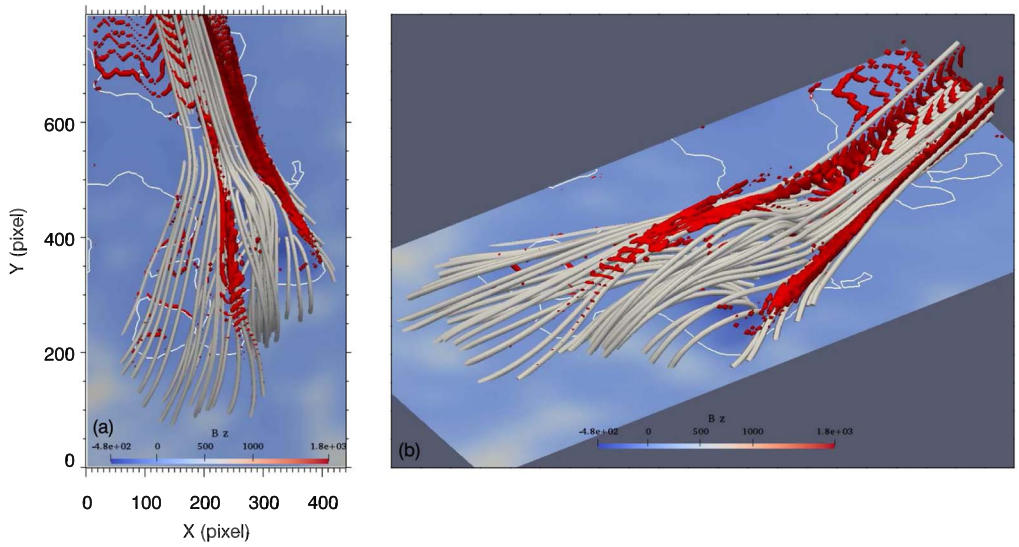

Figure 7. Magnetic topology for the small-scale jet through the NLFFF extrapolation. Panel (a) shows the magnetic topology in the X–Y plane seen from the Z-direction, and panel (b) shows a 3D perspective. The white contours in panels (a) and (b) indicate the PIL. The red surfaces represent the 3D high-Q ($\log Q = 3.5$) surfaces based on the NLFFF extrapolation, and the color bars display the B_Z on the bottom boundary in the extrapolated area.

the initial cool ejections from intergranular lanes get immediately excited. This result is similar to the relationship between 10830 Å absorption in the sunspot area and EUV emissions from an M-class flare (Wang et al. 2016). However, for this jet event, collision processes (collision ionization and collision excitation) should be taken into account at the early phases of each stage considering the first-step magnetic reconnection in the lower atmosphere. At the bottom of the jet's base, we observe bright kernels in 10830 Å, which may be related to the heating process due to magnetic energy release in the chromosphere during the first-step reconnection. Huang et al. (2020) also reported that absorption in the 10830 Å line turns into emission as heating time increases in flare models based on non-LTE calculation.

Long-lasting flux emergence for hours or days is common in the solar atmosphere, often associated with the formation of active regions. The spatial scale reaches hundreds of megameters. In the early phase of its evolution, an active region at the chromosphere is characterized by the presence of an arch filament system (AFS; Bruzek 1967; Tsiropoula et al. 1992). Meanwhile, small-scale flux emergence inside granules occurs frequently. When they pass through the photosphere, they manifest as increased brightness, bright pointlike features, or filament-like structures (Yurchyshyn et al. 2012). For this jet event, we find that the flux emergence lasts for $\geqslant$50 minutes before the appearance (or occurrence) of the jet. The photospheric counterpart shows filamentary structures with bright points in the TiO images. As is shown in Figure 4, the region of interest presents small filament-like features. These transient features usually develop rapidly and have bright points at the ends. The length of the individual filamentary structure is about $(1.5-2) \times 10^3$ km. For the magnetogram, the region corresponds to a small patch of the negative field with a size of 3 Mm × 3 Mm.

Cheung et al. (2008) interpreted the transient darkening as cool plasma descending into the photosphere. However, the bright components may be associated with upflows pushed by rising flux tubes. Lim et al. (2011) reported that elongated granule-like features observed in TiO images are related to flux emergence, accompanied by different chromospheric behavior due to different magnetic topology. Horizontal vortex tubes, which may be related to enhanced small-scale fields, are reported to be at the origin of small intergranular jets (Goode et al. 2010b; Yurchyshyn et al. 2011). Such fine-scale structures need further investigation with high-resolution observations.

The jet is composed of hot and cool components (e.g., Mulay et al. 2017). The cool component shows absorption in 10830 Å in its dome-shaped base and in the inclined spire. It is actually made up of numerous dark threads. We can obtain the widths of separated dark threads. Due to the overlap of numerous dark threads, we chose distinctly isolated threads whose cross-sectional intensity profiles present Gaussian distribution. As shown in the representative examples in Figure 8, the Gaussian FWHMs of the dark threads range from 176.6 km to 205.1 km for the jet base (panels (L1)–(L4)) and from 139.3 km to 250.2 km for the jet spire (panels (L5)–(L8)). Generally, the He I 10830 Å line is optically thin. Thus, the granulations in the photosphere emit through as the background of the chromospheric jet in the 10830 Å images. By comparing observations from He I 10830 Å and TiO 7057 Å, we find that the thin dark threads are rooted in the photospheric intergranular lane. A few examples are marked with plus signs in panels (a2) and (b2) of Figure 1. The width of the intergranular lanes is equal to the size of the cross section of the 10830 Å absorption threads, which is consistent with the picture that the fine threads are rooted in intergranular lanes.

Photospheric activity below the jet is rich, and we believe that it plays an important role in triggering the jet. Before the occurrence of the jet, a few negative poles converge and move toward the PIL with a speed of 150 km s^{-1}. Based on the TiO evolution, the photospheric flow pushes the penumbra-like structure and moves toward the PIL at a speed of ~100 km s^{-1}. Based on the observation of the TiO and magnetic field, the photospheric motions converge toward the PIL; this favors the formation of a nearly vertical current sheet (Titov et al. 1993). Using the result of the NLFFF extrapolation, we find the presence of a bald patch, which is a key topological feature for the jet. Mandrini et al. (2002) reported surges and AFSs in the magnetic topology of bald patches. Magnetic reconnection is

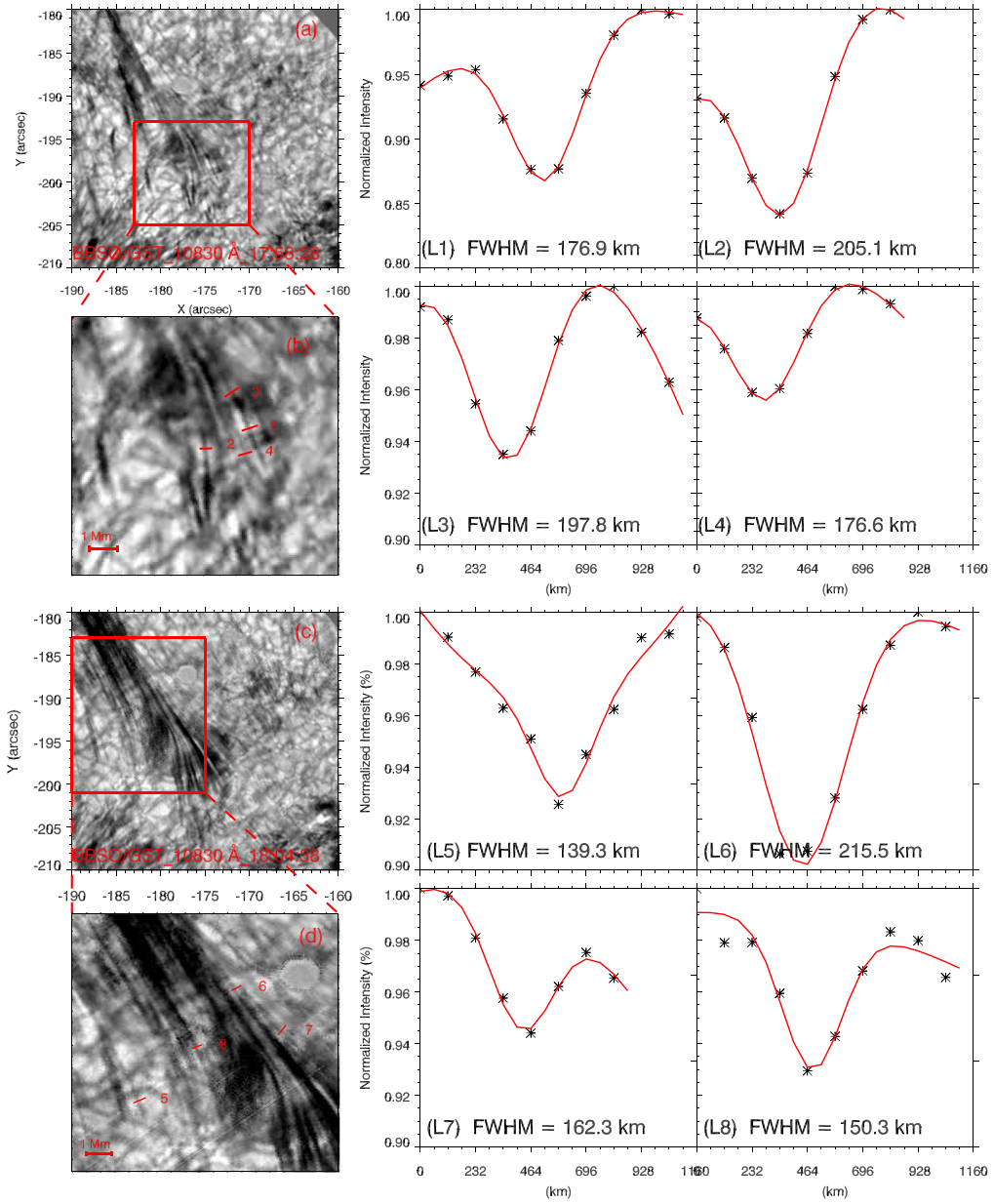

Figure 8. A series Gaussian fitting to get the width of the dark threads from the two images given in panels (a) and (c) or the enlarged ones given in panels (b) and (d). Panels (L1)–(L8) give the normalized intensity profiles (asterisks) of the slits across the isolated 10830 Å dark threads shown in panels (b) and (d). The result of the corresponding Gaussian FWHM is labeled in each panel.

expected to occur along the separatrices associated with the bald patch, and the photospheric motions can drive the formation of current sheets in the bald patch (Titov & Démoulin 1999). As shown in Figure 2, we observe brightening at the bottom of the dome at the beginning of the jet in 1600 Å (panels (a2) and (b2)). Correspondingly, it shows enhanced absorption in 10830 Å at 17:51:08 UT and turns into emission at 17:56:16 UT under the dome-like structure.

Besides, the magnetic topology obtained from the NLFFF extrapolation agrees with the observation, as shown in Figure 7. We investigated magnetic connectivities by tracing the squashing factor Q of the field lines, using the method by Liu et al. (2016). The Q factor is useful for mapping the boundaries between different magnetic regions (Titov et al. 2002). Figure 9 displays the log Q map (left panel) and its cross section along the dashed line (right panel). The shape of the high-Q line is consistent with the observed dome and spire. Magnetic reconnection occurs preferably in the high-Q region, which is indicated by a red arrow in Figure 9. Joshi et al. (2020) suggested that the bald-patch current sheet is formed above the bald patch when the negative polarity travels close to the positive one. However, we suggest that the jet starts due to magnetic reconnection around the quasi-separatrix layer associated with the bald patch. All of the above supports the observation that magnetic reconnection takes place in the lower atmosphere as the driver of first-step activity.

Above the brightening, the inverted Y structure is distinct as indicated in Figure 2. From the 10830 Å counterpart, we observe the thin threads at the dome of the jet transform from arc-shaped magnetic arcades into newly formed magnetic lines after reconnection as displayed in panels (c1)–(d1). Meanwhile, the downflow moves toward the footpoint, and the upflow

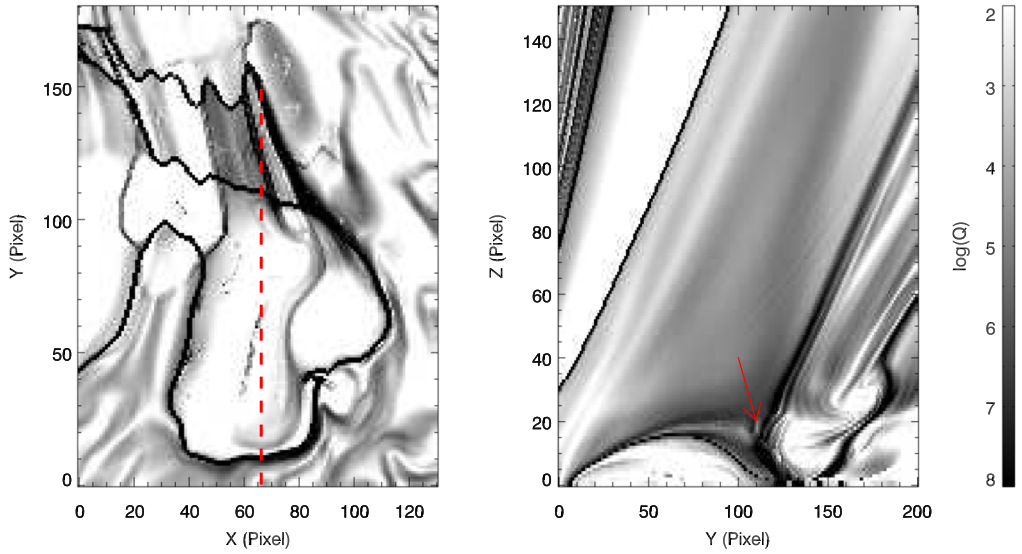

Figure 9. Left panel: map of the squashing factor Q in the X–Y plane at $Z = 2$ calculated from the NLFFF extrapolation. Right panel: maps of Q slices in the Y–Z plane with two different Y values. The red arrow refers to the high-Q region, where magnetic reconnection may occur.

shows up as a jet along the open magnetic field lines. Mandrini et al. (2002) also reported that part of the plasma can be compressed and injected into new and longer field lines during the reconnection process, while a large amount can escape downward. Recently, Yang et al. (2020) reported that when magnetic reconnection occurs at the null point, some dark materials are ejected from the reconnection site and moved along the fan dome and spine lines. Correspondingly, they observed blueshift and redshift in Hα dopplergrams and an enhanced blue wing and red wing in the Si IV line profile.

For each stage of the jet, two-step magnetic reconnection can be assumed: one is in the lower atmosphere, probably the photosphere, while another is in or above the chromosphere. In Figure 10, we draw a conceptual cartoon to show the magnetic reconnection of the jet, though the real situation is much more complex. In the left panel, a U-shaped loop associated with the bald patch reconnects at the intersection point (yellow star), which is probably driven by photospheric convection. The reconnection generates a downward-moving plasmoid and local heating and upward flows. The upward flows may constitute the initial dominant cool flows seen in 10830 Å. In the right panel, the plasmoid moves upward, due to the magnetic buoyancy force. The plasmoid further reconnects with the horizontal field lines, producing bidirectional flows. The second-step magnetic reconnection produces a new U-shaped loop, which can be driven to reconnect again. Therefore, the cartoon not only explains the two-step magnetic reconnection but also predicts the periodicity of the reconnection, which is consistent with the recurrent behavior of the jet.

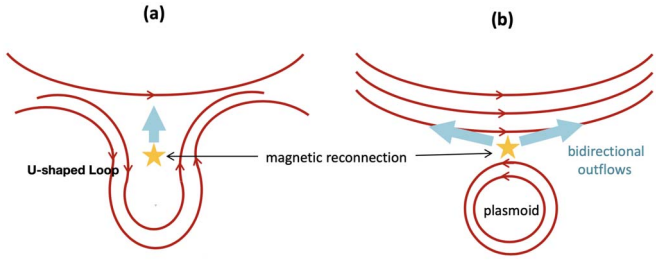

Figure 10. Schematic cartoon showing the magnetic reconnection in a bald-patch magnetic configuration. Left panel: a U-shaped loop reconnects at the intersection point (yellow star) driven by photospheric convection and produces a plasmoid and bidirectional flows. Right panel: the plasmoid moves upward due to buoyancy and reconnects with the horizontal field lines, producing bidirectional flows. See text for details.

5. Summary

With high-resolution narrowband He I 10830 Å and broadband TiO 7057 Å images observed by the 1.6 m aperture GST at BBSO, aided by high-quality EUV/UV images from AIA on board SDO, we are able to give a detailed analysis of the dynamic characteristics of the small-scale jet from emission (including absorption), the morphology and the movement of both cool and hot components, and the evolution of the associated photosphere and magnetic field. The main results are summarized as follows:

(1) The jet shows the coexistence of multi-temperature components, observed in the 10830 Å, 1700 Å, 1600 Å, and EUV passbands. However, they are neither co-temporal nor co-spatial, presenting different speed characteristics in different temperature ranges. The chromospheric counterpart displays fine structures. Both the spire and the base of the jet are made of thin dark threads. The widths of isolated threads range from 139.3 km to 250.2 km. The thin dark threads are rooted in the intergranular lanes.

(2) The jet presents a collimated-like morphology and looks like an inverted Y structure as observed in the hot component. The jet starts earlier in the low-temperature passband (10830 and 1600 Å) with lower speeds than in the coronal temperatures. Also, there is a separate bright kernel under the inverted Y structure in the low-temperature passband.

(3) Under the jet, photospheric activity is rich, which is indicated by flows, magnetic emergence, and flux cancellation. The horizontal magnetic field is enhanced during the jet, and its configuration indicates the existence of a bald-patch magnetic topology. Based on the photospheric evolution and magnetic topology, we suggest that the formation of the jet is due to magnetic reconnection in a bald-patch topology driven by

photospheric motion. We propose that magnetic reconnection in a bald-patch topology has a tendency to recur.

We thank the anonymous referee for comments that improved the paper. We thank the team of SDO/AIA and SDO/HMI for providing the valuable data. The AIA and HMI data were downloaded via the Joint Science Operations Center. BBSO operation is supported by NJIT and US NSF AGS-1821294 grant. GST operation is partly supported by the Korea Astronomy and Space Science Institute, the Seoul National University, and the Key Laboratory of Solar Activities of Chinese Academy of Sciences (CAS) and the Operation, Maintenance and Upgrading Fund of CAS for Astronomical Telescopes and Facility Instruments. We thank Thomas Wiegelmann for sharing the NLFFF code. We thank Kai Yang and Jincheng Wang for discussing the magnetic topology and guiding plotting of three dimension magnetic field. Thank Rui Liu for sharing the Q factor calculation program. This work is supported by NSFC grants 12003072, 11790302, and 11773079. Y.W. is supported by the Youth Fund of JiangSu (No. BK20191108), and the Key Laboratory for Modern Astronomy and Astrophysics (Nanjing University), Ministry of Education. Q.Z. is supported by the CAS Key Laboratory of Solar Activity, National Astronomical Observatories (KLSA202006), and the Youth Innovation Promotion Association of CAS.

ORCID iDs

Ya Wang https://orcid.org/0000-0003-3699-4986
Qingmin Zhang https://orcid.org/0000-0003-4078-2265

References

Bai, X. Y., Su, J. T., Cao, W. D., et al. 2016, ApJ, 823, 60
Bruzek, A. 1967, SoPh, 2, 451
Cao, W., Coulter, R., Gorceix, N., et al. 2010a, Proc. SPIE, 7742, 774220
Cao, W., Gorceix, N., Coulter, R., et al. 2010b, AN, 331, 636
Cheung, M. C. M., De Pontieu, B., Tarbell, T. D., et al. 2015, ApJ, 801, 83
Cheung, M. C. M., Schüssler, M., Tarbell, T. D., et al. 2008, ApJ, 687, 1373
Ding, M. D., Liu, Y., Yeh, C.-T., et al. 2003, A&A, 403, 1151
Golding, T. P., Carlsson, M., & Leenaarts, J. 2014, ApJ, 784, 30
Goode, P. R., Coulter, R., Gorceix, N., et al. 2010a, AN, 331, 620
Goode, P. R., Yurchyshyn, V., Cao, W., et al. 2010b, ApJL, 714, L31
Guo, Y., Démoulin, P., Schmieder, B., et al. 2013, A&A, 555, A19
Hashim, P., Hong, Z., Ji, H., et al. 2020, arXiv:2010.06787
Hong, Z.-X., Yang, X., Wang, Y., et al. 2017, RAA, 17, 25
Hu, Y. K., Xu, Z., Xue, Z. K., et al. 2015, AcASn, 56, 579
Huang, N., Sadykov, V. M., Xu, Y., et al. 2020, ApJL, 897, L6
Ji, H., Cao, W., & Goode, P. R. 2012, ApJL, 750, L25
Jiang, Y. C., Chen, H. D., Li, K. J., et al. 2007, A&A, 469, 331
Joshi, R., Schmieder, B., Aulanier, G., et al. 2020, A&A, 642, A169
Kim, Y.-H., Moon, Y.-J., Park, Y.-D., et al. 2007, PASJ, 59, S763
Leka, K. D., Barnes, G., Crouch, A. D., et al. 2009, SoPh, 260, 83
Lemen, J. R., Title, A. M., Akin, D. J., et al. 2012, SoPh, 275, 17
Lim, E.-K., Yurchyshyn, V., Abramenko, V., et al. 2011, ApJ, 740, 82
Liu, J., Wang, Y., Erdélyi, R., et al. 2016, ApJ, 833, 150
Liu, S., & Su, J. T. 2018, SoPh, 293, 167
Liu, W., Berger, T. E., Title, A. M., et al. 2011, ApJ, 728, 103
Mandrini, C. H., Démoulin, P., Schmieder, B., et al. 2002, A&A, 391, 317
Metcalf, T. R., Leka, K. D., Barnes, G., et al. 2006, SoPh, 237, 267
Mulay, S. M., Del Zanna, G., & Mason, H. 2017, A&A, 606, A4
Nishizuka, N., Nakamura, T., Kawate, T., et al. 2011, ApJ, 731, 43
Nisticò, G., Bothmer, V., Patsourakos, S., et al. 2009, SoPh, 259, 87
Panesar, N. K., Sterling, A. C., Moore, R. L., et al. 2016, ApJL, 832, L7
Panesar, N. K., Sterling, A. C., & Moore, R. L. 2018, ApJ, 853, 189
Raouafi, N. E., Patsourakos, S., Pariat, E., et al. 2016, SSRv, 201, 1
Roy, J.-R. 1973a, SoPh, 32, 139
Roy, J. R. 1973b, SoPh, 28, 95
Rust, D. M. 1968, in IAU Symp. 35, Structure and Development of Solar Active Regions, ed. K. O. Kiepenheuer (Dordrecht: D. Reidel), 77
Schou, J., Scherrer, P. H., Bush, R. I., et al. 2012, SoPh, 275, 229
Schuck, P. W. 2008, ApJ, 683, 1134
Shen, Y. 2021, RSPSA, 477, 217
Shen, Y., Liu, Y., Su, J., et al. 2012, ApJ, 745, 164
Shibata, K., Nakamura, T., Matsumoto, T., et al. 2007, Sci, 318, 1591
Shimojo, M., Hashimoto, S., Shibata, K., et al. 1996, PASJ, 48, 123
Shimojo, M., Shibata, K., & Harvey, K. L. 1998, SoPh, 178, 379
Sterling, A. C., Moore, R. L., & Panesar, N. K. 2018, ApJ, 864, 68
Su, J. T., Ji, K. F., Banerjee, D., et al. 2016, ApJ, 816, 30
Tian, H., DeLuca, E. E., Cranmer, S. R., et al. 2014, Sci, 346, 1255711
Titov, V. S., & Démoulin, P. 1999, A&A, 351, 707
Titov, V. S., Hornig, G., & Démoulin, P. 2002, JGRA, 107, 1164
Titov, V. S., Priest, E. R., & Demoulin, P. 1993, A&A, 276, 564
Tsiropoula, G., Georgakilas, A. A., Alissandrakis, C. E., et al. 1992, A&A, 262, 587
Wang, Y., Su, Y., Hong, Z., et al. 2016, ApJ, 833, 250
Welsch, B. T., Fisher, G. H., Abbett, W. P., et al. 2004, ApJ, 610, 1148
Wheatland, M. S., Sturrock, P. A., & Roumeliotis, G. 2000, ApJ, 540, 1150
Wiegelmann, T. 2004, SoPh, 219, 87
Yang, S., Zhang, Q., Xu, Z., et al. 2020, ApJ, 898, 101
Yurchyshyn, V., Ahn, K., Abramenko, V., et al. 2012, arXiv:1207.6418
Yurchyshyn, V. B., Goode, P. R., Abramenko, V. I., et al. 2011, ApJL, 736, L35
Zeng, Z., Cao, W., & Ji, H. 2013, ApJL, 769, L33
Zeng, Z., Chen, B., Ji, H., Goode, P. R., & Cao, W. 2016, ApJL, 819, L3
Zhang, Q. M., & Ji, H. S. 2014, A&A, 567, A11
Zhang, Y., & Zhang, J. 2017, ApJ, 834, 79
Zirin, H. 1975, ApJL, 199, L63